Bulletin of the Seismological Society of America, Vol. 75, No. 4, pp. 1005–1020, August 1985

# IMAGING OF EARTHQUAKE SOURCES IN LONG VALLEY CALDERA, CALIFORNIA, 1983

BY GEORGE A. MCMECHAN, J. H. LUETGERT, AND W. D. MOONEY

## ABSTRACT

**A finite difference technique by which an earthquake wave field recorded at the Earth's surface could be extrapolated backward in time to produce an image of the source was presented by McMechan (1982). The resulting image is dynamic and reveals the temporal and spatial configuration of the acoustic equivalent of the source. The method was successfully tested on synthetic data, but no real earthquake data satisfying the prerequisites for processing were available in 1982. The data must be recorded close to the source and must be spatially dense. In January of 1983, a unique data set was recorded by the U.S. Geological Survey within Long Valley Caldera in eastern California. Three events were chosen from the aftershock sequence. Preprocessing of the data for each event includes construction of a true amplitude section, filtering, and extrapolation to produce unaliased, equally spaced observations. Extrapolation of these data through a previously determined velocity structure produces coherent images in which both the source location and radiation pattern are visible. The images are also consistent with previously determined focal mechanisms. The results demonstrate the feasibility of imaging real earthquake sources.**

## INTRODUCTION

The concept of migration is familiar to seismologists working in reflection seismology where the imaging of Earth reflectivity (structure) is a major goal. Recently, McMechan (1982) showed that, with some changes in recording geometry, earthquake data can be used to form an image of the earthquake source. The fundamental idea that links these two very different applications is that a diffractor or reflector can be thought of as being composed of a spatial distribution of secondary point sources. In reflection seismology, this is called the exploding reflector model and in application to earthquake data the point sources are associated with a fault plane (a primary source) rather than a diffractor (a secondary source).

Migration consists of two distinct elements; a method for extrapolation of the time-distance ($T$-$x$) observations plus an imaging condition to stop extrapolation. Extrapolation is generally performed in depth ($z$) such that data from the $T$-$x$ domain become imaged in the distance-depth ($x$-$z$) domain. The imaging condition is generally derived from the exploding reflector model. In particular, the energy imaged at each $z$ slice is that which corresponds to time = 0 in the extrapolated ($T$-$x$) wave field (Claerbout, 1976).

The idea of imaging earthquake data has grown from a consideration of migration in the novel form of extrapolation in time rather than in depth (although depth extrapolation works equally well for this application). To date, the application of "reverse time migration" is more widespread in reflection seismology than in earthquake seismology only because of the availability of relevant data. Recent papers that discuss this approach in the context of extrapolation seismology are: McMechan (1983); Whitmore (1983); Kosloff and Baysal (1983); Loewenthal and Mufti (1983); Baysal *et al.* (1983, 1984); and Levin (1984). The conceptual basis is, however, much older. For example, graphical extrapolation of wave fronts in time is discussed by Thornburgh (1930), Gardner (1949), Baumgarte (1955), Hales (1958), Hagedoorn (1959), Rockwell (1967), Schenck (1967), and Telford *et al.* (1976). Kennett (1983) has discussed the application to earthquake data.

Following the main shocks of the 7 January 1983 earthquakes in the Long Valley region of east-central California, several aftershocks were recorded with a dense seismograph array by the U.S. Geological Survey (USGS). We selected three of the largest recorded aftershocks (Figure 1) for imaging based on event size and a preliminary location near the recording array. Images formed by the processing of these data are the main result of this paper.

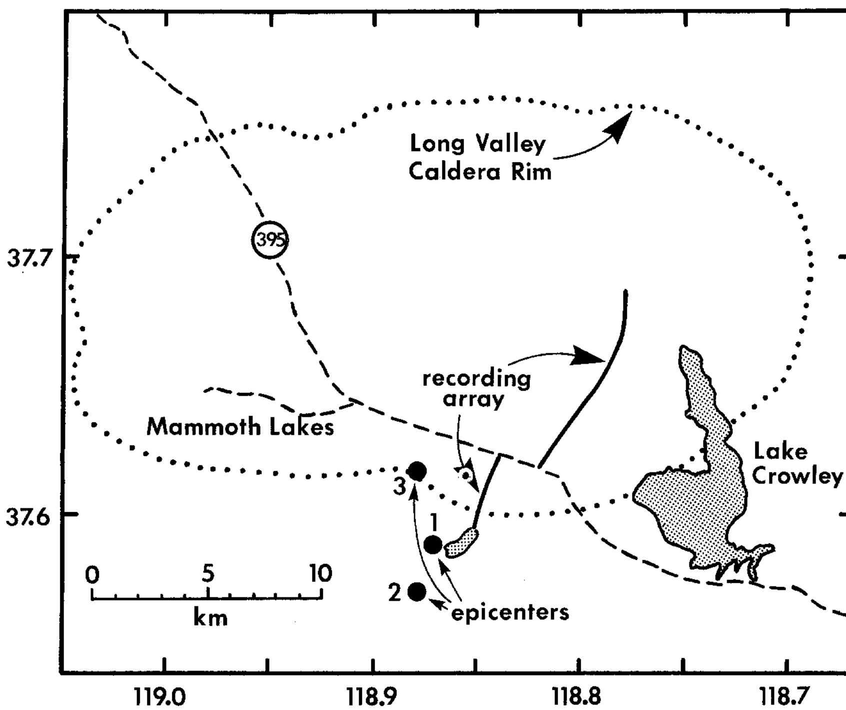


FIG. 1. Location map of earthquake epicenters (large dots) relative to the recording array (solid lines) and the Long Valley Caldera (dotted line). Data from the earthquakes are extrapolated to produce the source images in Figures 4, 7, and 9. Hypocentral information is given in Table 1.

## LONG VALLEY DATA

On 7 January 1983, an intense earthquake swarm began in southwestern Long Valley and the adjacent Sierra Nevadan block. The largest two events in the swarm had magnitudes ($m_b$) 5.3 and 5.6. Over 400 events with a magnitude greater than $m_b$ = 1.5 were recorded during the first 3 hr by the permanent regional network operated by the USGS (Pitt and Cockerham, 1983). During the earthquake swarm, the USGS deployed 120 portable seismographs along two separate lines in the vicinity of Long Valley-Mono Craters of east-central California. A total of 50 earthquakes of magnitude greater than $m_b$ = 0.5 were recorded on these two linear arrays during a total of 2 hr of recording time. Figure 1 shows the location of the roughly NE-SW recording line within Long Valley Caldera discussed here. Records from the second deployment in the vicinity of Mono Craters, NNW of Long Valley caldera, are discussed by Luetgert and Mooney (1985).

The Long Valley Caldera (Figure 1) is an elliptical depression which lies at the eastern margin of the Sierra Nevada 30 km south of Mono Lake. The caldera formed from the collapse of the Long Valley magma chambers following the explosive eruption that produced the Bishop tuff 0.7 m.y. ago (Bailey *et al.*, 1976). The basement rocks in the immediate area of Long Valley are Jurassic and Cretaceous granodiorites and granites of the Sierra Nevada batholith, and Paleozoic and Mesozoic metamorphic rocks of the Mount Morrison and Ritter range roof pendants. Overlying the basement rocks are late Tertiary volcanic rocks, mainly basalt, andesite, and rhyodacite (Bailey *et al.*, 1976). Regional seismic refraction studies (Johnson, 1965; Eaton, 1966; Prodehl, 1979) provide a broad view of the crustal velocity structure in the area of eastern California and western Nevada, showing that the crust in the Long Valley area consists of essentially three layers. Beneath a surficial layer of volcanic and fractured metamorphic rocks, there is a layer in which the *P*-wave velocity increases gradually from 6.0 to 6.2 km/sec at a depth of 2 to 4 km to 6.4 km/sec at a depth of 25 to 30 km. Velocities of 6.8 to 7.2 km/sec are measured in the lowest 10 to 20 km of the crust (~30 to 40 km depth). Within the context of this regional velocity distribution, there is of course considerable local variation, especially within the upper 2 km associated with the caldera (Hill, 1976). For the area considered here, which transects the southern rim of the caldera, our velocity model must reflect the transition from the relatively low velocities of the volcanic rocks forming the caldera fill to the higher velocities in the crystalline basement of the Sierran Block. The specific two-dimensional velocity distribution used for the wave field extrapolation of the earthquake data is a composite of two one-dimensional models that have been determined from recent studies localized in the area of interest here. For the Sierra region, the profile shown in Figure 2a was used; this was obtained by E. Kissling (personal communication, 1983) using the method of Crosson (1976) for joint simultaneous inversion of earthquake travel times for hypocenters and a one-dimensional velocity model. For the Long Valley Caldera region, the profile shown in Figure 2b was used; this was obtained by inversion of refraction data collected in 1983. These two one-dimensional models are joined smoothly beneath the caldera rim. Recently, more precise determinations of the velocity structure within and adjacent to the Long Valley Caldera have been made (Hill *et al.*, 1985; Kissling *et al.*, 1985), but the differences from the preliminary models we have used would not seriously alter our results.

Recent high seismicity and the potential for volcanic activity have stimulated interest in investigations of velocity structure, earthquake location, and focal mechanisms in and around Long Valley. Examples include Cramer and Toppozada (1980), Savage *et al.* (1981), Ryall and Ryall (1981), Given *et al.* (1982), Hartzell (1982), Barker and Langston (1983), and Priestly *et al.* (1984). Our strategy in the present experiment was to take advantage of the high seismicity level during the January 1983 swarm to record earthquake profiles with a densely spaced linear array for use in finite difference source imaging.

The portable seismographs were equipped with single vertical-component velocity transducer with a natural resonance at 2 Hz. Recorder spacing was 100 m, with an estimated location accuracy of ±5 m. Seismic record sections were prepared by digitizing the analog tapes at 200 samples/sec.

The three earthquakes used in this study (Figure 1) were selected on the basis of their being the largest aftershocks recorded during the two 30-min recording periods that were located near the southwestern end of the recording array. The hypocentral information for these events, which were located beneath the southern edge of Long Valley Caldera, is given in Table 1.

## PREPROCESSING OF DATA

Extensive preprocessing is required to prepare raw earthquake data for imaging by a finite difference extrapolation backward in time. The necessary steps include construction of a true amplitude section (so that the source radiation pattern can be observed in the image), filtering (so the data are relatively noise free and

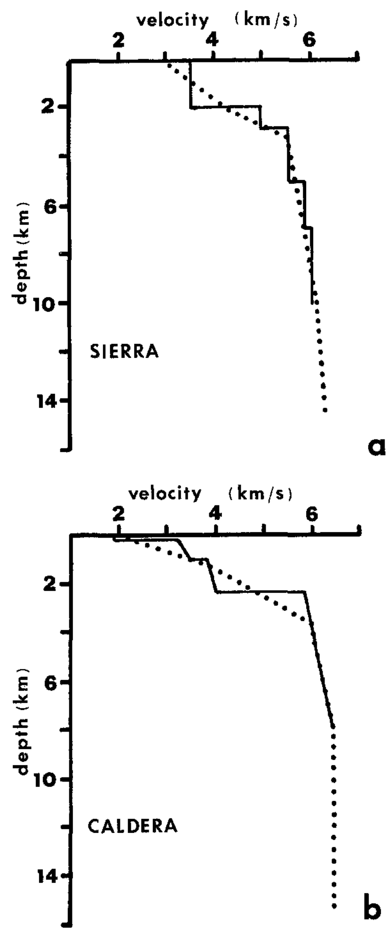


FIG. 2. One-dimensional velocity profiles for the Sierra Nevada region (a) and the Long Valley Caldera (b). The smoothed profiles (dotted lines) are combined into a two-dimensional model through which wave field extrapolation is performed.

unaliased), and interpolation (to produce a data profile at equally spaced observation points that correspond to the finite difference grid lines). In this section, each of these three steps is discussed in turn.

The first step in data preprocessing (after the usual digitization, editing, and time corrections) is the recovery of true amplitudes. Because the filtering in the second step involves a relatively narrow band, we do not attempt deconvolution of the instrument response. We make two corrections; the first for the gain of each instrument and the second, for receiver directivity. It is not necessary to correct for the free surface effect as this is implicitly included in the finite difference boundary conditions. The directivity correction is required because the wave field extrapolation uses the acoustic wave equation, and the data are for the vertical component only. This correction is approximate and involves division of each trace by the cosine of the incident angle of the ray corresponding to the first arrival on that trace. In practice, imaging was first performed without the directivity correction to determine the source location. Once the approximate source location was established, the directivity correction could be reliably estimated, applied to the data, and a final corrected image obtained. Finally, each trace is integrated to displacement to enhance the lower frequency contributions. All the following processes are performed on the displacement traces.

The second step in preprocessing is to apply a bandpass filter to each of the data traces. The reasons for filtering are three-fold: noise is reduced; removal of high frequencies reduces grid dispersion in the finite difference extrapolation; and spatial and temporal aliasing is reduced which increases the reliability of extrapolation between data traces. In this study, we used a bandpass of 1 to 10 Hz (in velocity).

Data interpolation is the most crucial (and potentially most controversial) element of preprocessing. Finite difference methods for extrapolation of wave fields to image earthquake data require that a trace be available at each free surface point

TABLE 1
SOURCE PARAMETERS FOR IMAGED EVENTS (R. S. COCKERHAM, PERSONAL COMMUNICATION, 1984)

| Event | Date | Latitude | Longitude | Origin Time (GMT) | Depth (km) | Magnitude ($m_b$) |
|---|---|---|---|---|---|---|
| 1 | 9 January 1983 | 37 35.33 | 118 52.20 | 06 26:27.83 | 13.34 | 1.42 |
| 2 | 9 January 1983 | 37 34.20 | 118 52.79 | 06 19:50.06 | 14.76 | 0.85 |
| 3 | 9 January 1983 | 37 37.08 | 118 52.74 | 10 01:08.09 | 6.18 | 1.45 |

on a computational grid, and this is only approximated by the physical recording geometry. A typical field recording array, while it may be roughly linear (assuming two-dimensional imaging is to be done) and spatially dense, usually cannot be extrapolated directly. Real data generally include a certain randomness in station location due to local siting difficulties, missing or unusable traces due to instrument malfunctions, and excessively noisy traces due to local factors (e.g., cultural noise). Even if the data do not contain such problems, the spacing between traces may be too great to obtain a stable finite difference solution at the frequencies of interest. We discuss this last point in more detail in the following section.

The first part of the extrapolation sequence is the computation of a reduced time profile. For this, we use the standard (linear) form of the reduction function

$$Tr = T - x/v \tag{1}$$

where $Tr$ is reduced time, $T$ is unreduced time, $x$ is distance, and $v$ is the reduction velocity. The reduction velocity $v$ is chosen so that the data are nowhere spatially aliased (at the dominant frequencies) after reduction. In some cases, it may be necessary to use a nonlinear time reduction function to ensure unaliased output. Interpolation is done in this unaliased profile and then the interpolated traces are returned (by time shifting) to their corresponding unreduced position.

The actual interpolation of an unaliased (reduced time) section is done in the frequency domain. To predict a trace at any distance $x_0$, the nearest two seismograms are found (one on each side of $x_0$). Then, the Fourier transform of the extrapolated trace is constructed by a linear interpolation between the Fourier coefficients (at each frequency in turn) of the two adjacent traces. An inverse Fourier transform then produces the predicted time trace. Because the data are unaliased in the reduced time format, stable extrapolation is achieved; amplitudes and phases vary smoothly in the interpolated wave field. The choice of interpolation scheme is arbitrary.

Any arrival branch can be interpolated in the distance dimension in this way provided reasonable caution is taken. In particular, one must bear in mind that: (1)

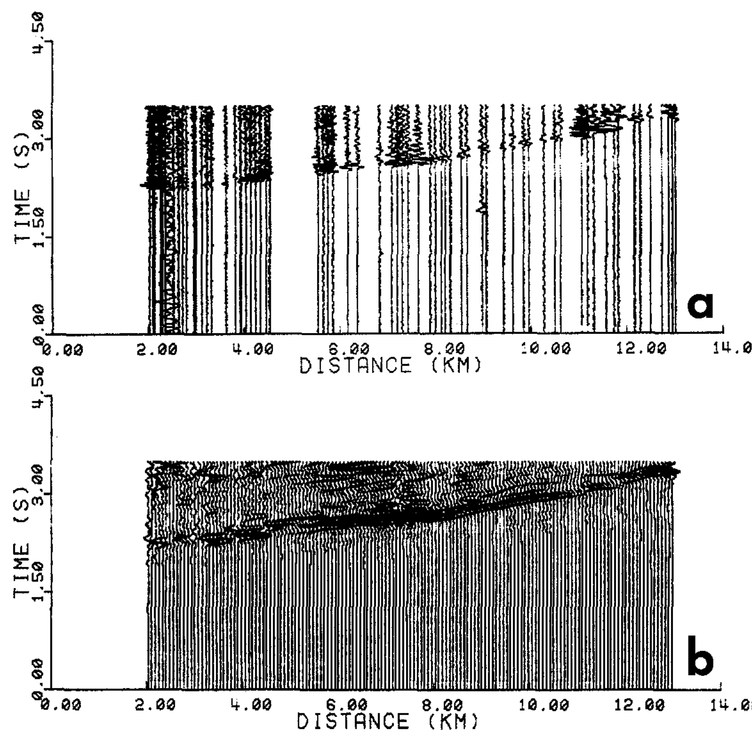


FIG. 3. Data from event 1. (a) Raw data. (b) True amplitude wave field after filtering and interpolation.

interpolation will be reasonable only for those frequencies that are not aliased in the reduced time profile; (2) a bad (noisy) trace will contaminate the interpolated wave field in its neighborhood; and (3) interpolation does not genereate new information (it simply redistributes the old). Finally, it should be noted that the filtering and interpolation operation can be combined so that the data need be Fourier transformed only once. This approach works well when only one arrival branch (i.e., a small range in slowness) is involved. When multiple branches with widely differing slownesses are to be interpolated simultaneously, some other algorithm (such as forward and inverse slant stacking) must be used.

Figure 3 contains the data from event 1 before and after preprocessing. Similarly, Figure 6 contains the data from event 2 and Figure 8 contains the data from event 3. The preprocessed data in these figures are displayed with 95 m trace separation.

For input to the extrapolation and imaging described in the following section, a 45 m trace separation is used. The raw data are displayed with no gain, time, or distance corrections and distances are approximate epicentral distances (computed from the preliminary hypocenters in Table 1). In the processed data, all the corrections described above have been applied, and distances are relative distances measured along the surface trace of the image plane. For the purpose of imaging, only the relative positions of the observations are required.

## Imaging of Data

The extrapolation of unaliased, equally spaced, synthetic seismic (earthquake) traces by a finite difference implementation of the acoustic wave equation has been demonstrated by McMechan (1982). The basic principle involved is that the wave equation is completely reversible in time. Seismograms serve as time-dependent boundary conditions, and the finite difference mesh is driven by the time reverse of the seismic trace at each recording point.

Until the Long Valley data were recorded, there were no natural earthquake data available to the authors that met the criteria for imaging. Even these data, however, are short of ideal. Nevertheless, with the extensive preprocessing described above, images can be obtained. Indeed, the main purpose of this paper is to demonstate the feasibility of imaging real earthquake data.

In finite difference imaging, there is a strong interaction between the data and the numerical algorithm. For example, the horizontal mesh increment is equal to the interpolated data trace separation and the time digitization increment of the data is equal to the time step in extrapolation. These quantities interact further in determining stability and grid dispersion characteristics in the extrapolation algorithm. We must, therefore, consider the implementation and the choice of parameters in some detail.

Energy is propagated through the finite difference grid according to the two-dimensional acoustic wave equation (Claerbout, 1976; Mitchell, 1969)

$$U_{xx} + U_{zz} = V^{-2}(x, z)U_{tt} \tag{2}$$

where $U$ is propagating wave field, $V$ is velocity, and subscripts denote partial derivatives with respect to $x$ (the horizontal coordinate), $z$ (the vertical coordinate), or $t$ (time). For the present application, equation (2) is implemented in a second order, explicit difference scheme. The characteristics of such schemes with respect to numerical stability and grid dispersion are discussed by, among others, Alford *et al.* (1974) and Mitchell (1969). For local stability, time steps $\Delta T$ must be less than $hV^{-1}2^{-1/2}$ where $h$ is the grid increment in both the $x$ and $z$ directions. The use of a $\Delta t$ close to this upper limit is optimal; it simultaneously minimizes both the number of time steps required and grid dispersion. In application to real data, $\Delta t$ is usually predetermined; $h$ is equal to the grid spacing in the data interpolation step (see the previous section) and can be easily changed.

In practice, the decisions regarding the computational parameters are straightforward, and the bottom line involves a trade-off between the grid spacing and the bandpass chosen for the filter. For the present data sets, we made the following decisions. First, the digitization increment ($\Delta t$) for the field data was set at 0.005 sec. Second, the maximum velocity (see Figure 2) is ~6.2 km/sec. Thus, from the stability criterion, $h$ must be greater than 0.0438 km, and we set it to 0.045 km. To avoid significant grid dispersion, it is usually necessary to have more than 10 grid points per wavelength (cf. Alford *et al.*, 1974). With a filter bandpass of 1 to 10 Hz and velocities between 2.0 and 6.2 km/sec (Figure 2), a grid increment of 0.045 km gives more than 10 grid points per wavelength on all combinations except the highest frequencies and lowest velocities (Table 2). For example, for a dominant frequency of 5 Hz and average velocity of 5 km/sec, we have 22 samples per wavelength, which is completely adequate. As frequencies increase or velocities decrease, $h$ must be decreased.

Because observations are generally limited to the surface of the Earth, only upgoing waves are recorded, and these are observed only over a finite aperture. If the wave field was observed over an infinite (complete three-dimensional) aperture, all energy, including secondary phases such as multiples and converted waves, could be extrapolated with an elastic finite difference solution. At velocity discontinuities, these waves coalesce into the simpler waves that generated them. With incomplete data, this merging does not occur. On the contrary, each discontinuity will generate unwanted secondary phases. It is, therefore, desirable to suppress the effects of sharp discontinuities. Two ways of doing this are to adjust densities at each velocity discontinuity so that there is no discontinuity in acoustic impedance (cf. Levin, 1984), or to simply use a smoothed velocity structure that does not contain discontinuities. For the present study, we have used the latter option; the smoothed velocity models are the dotted lines in Figure 2.

TABLE 2

REPRESENTATIVE VALUES OF THE NUMBER OF SPATIAL SAMPLES PER WAVELENGTH AS A FUNCTION OF FREQUENCY AND VELOCITY

| Frequency (Hz) | Velocity (km/sec) | Samples/$\lambda$ |
|---|---|---|
| 1.0 | 2.0 | 44.0 |
| 10.0 | 2.0 | 4.4 |
| 1.0 | 6.2 | 137.0 |
| 10.0 | 6.2 | 13.8 |
| 5.0 | 5.0 | 22.0 |

The imaging process itself has been previously described in detail by McMechan (1982). The time step in extrapolation equals the time digitization increment in the data ($\Delta T = 0.005$ sec). At each iteration (each time step), the wave equation moves all the energy in the $x$-$z$ plane away from the upper ($z = 0$) boundary toward the source (image) position, and new boundary conditions are inserted at $z = 0$. The boundary values to be inserted at time $t_i$ are found in the seismogram profile along the slice at time $t_i$. Thus, extrapolation is performed by driving the mesh at each recording point with the time reverse of the seismic trace recorded at that point. Extrapolation continues backward in time until the origin time. The origin time, in the present context, is defined as the time at which the best-focused image is obtained. The $x$-$z$ wave field can be observed at any time step or sequence of time steps to see the movement of energy toward the source location and the associated focusing. For example, Figure 4 shows four wave fields generated by extrapolation of the data of event 1 (Figure 3b). Similarly, Figure 7 shows extrapolation of event 2 (Figure 5b) and Figure 9 shows extrapolation of event 3 (Figure 8b). These are discussed in the following section.

## PRESENTATION AND DISCUSSION OF RESULTS

The extrapolation and imaging of data from events 1, 2, and 3 (Figure 1, Table 1) are shown in Figures 4, 7, and 9, respectively. In this section, we discuss each of these examples in turn.

The extrapolation of data from event 1 is shown in Figure 4. In this figure, each panel is a snapshot of the wave field in a vertical slice through the Earth at some chosen time step. Figure 4, a to c, shows the first arrival branch (indicated by the

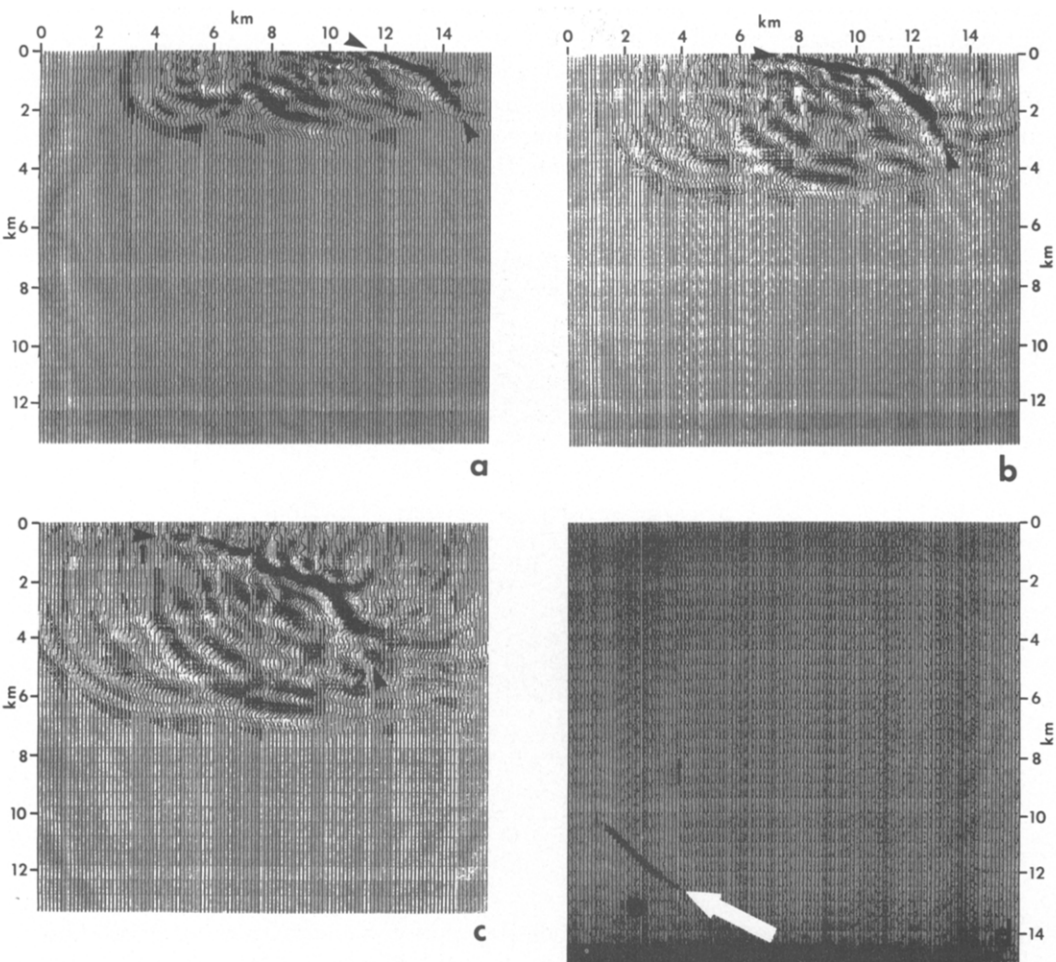


FIG. 4. Extrapolation and imaging of event 1. Panel (a) corresponds to 150 time steps, (b) to 300, (c) to 450, and (d) to 700. Each time step is 0.005 sec. The large arrow in (d) points to the "best"-focused source image. Arrowheads in (a), (b), and (c) indicate previous image positions. The round black dot in (d) is the preliminary hypocenter determined from regional network travel time. In (d), amplitudes are cubed before plotting to enhance the image.

small arrows) and its movement into the $x$-$z$ plane. Propagation backward in time to the origin time produces the focused source image indicated by the white arrow in Figure 4d.

The source radiation pattern is clearly visible in Figure 4c; amplitudes are minimum in the region vertically above the source (near arrow 1) and they increase with increasing angle from vertical. Also, the image is truncated near arrow 2 due to the finite recording aperture. Because the amplitude is significant at the large-distance edge of the recording aperture (at ~13 km in Figure 3b), finite difference extrapolation will produce a diffraction artifact in the image. To reduce this edge effect, a linear ramp taper was applied, over distance, at both aperture edges (for all data sets). Figure 5 illustrates the effectiveness of this method of edge effect suppression.

Data from the second event are shown in Figure 6. The extrapolation of these data, in the vertical plane, is shown in Figure 7, and the resulting source image is shown in Figure 7c. Data from the third event are shown in Figure 8, and the corresponding image is shown in Figure 9.

The third example differs from the previous two in that the source lies out of the vertical plane that contains the recording array. In all three examples, the image plane contains the source point and the recording array line. In the first two examples, this plane is essentially vertical as the events are in line with the recording

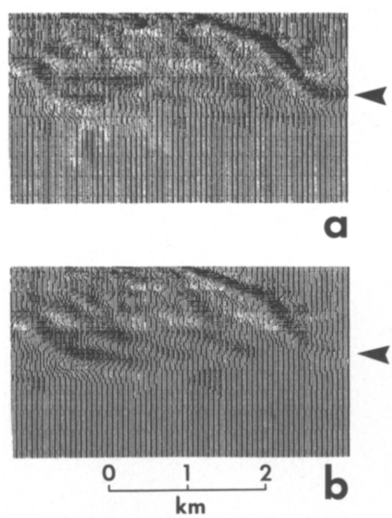


FIG. 5. Suppression of edge effects. This figure contains an enlarged portion (the *upper right corner*) of the same plane shown in Figure 4a. (a) The plane produced without data tapering and exhibits a strong diffraction artifact indicated by the arrowhead. In (b), data tapering has significantly reduced the artifact.

array. For the third event, however, which does not coincide with an extension of the recording profile (Figure 1), the appropriate plane dips at ~57.3° to the northwest. In confining extrapolation of the wave field from the surface to the source to this plane, we assume that the corresponding ray paths lie in the neighborhood of this plane. The validity of this assumption is reduced when the plane becomes farther from vertical and when significant lateral velocity variation is present. If the algorithm were implemented in three-dimensional form, this point would no longer be relevant. Each of our images differs in location from the hypocenters determined by the USGS regional network (the large black dots in Figures 4d, 7c, and 9) by 1 to 2 km. This is not unexpected, as different velocity models were used in the two methods. Note also that, in general, the image plane does not correspond to the fault plane.

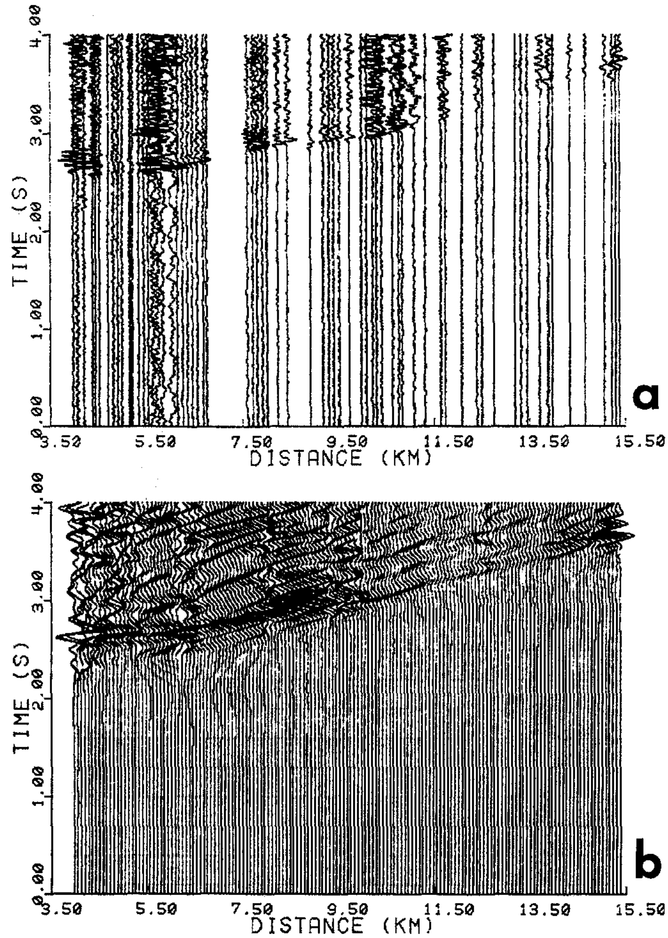


FIG. 6. Data from event 2. (a) Raw data. (b) True amplitude wave field after filtering and interpolation.

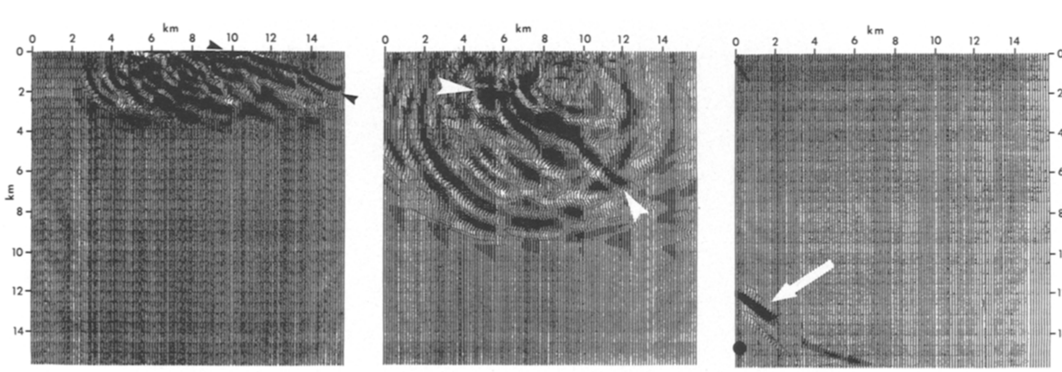


FIG. 7. Extrapolation and imaging of event 2. (a) Corresponds to 200 time steps, (b) to 500, and (c) to 800. The large arrow in (c) points to the best-focused source image. The arrowheads in (a) and (b) indicate previous image positions. The round black dot in (c) is the preliminary hypocenter determined from regional network travel times. In (c), amplitudes are cubed before plotting to enhance the image.

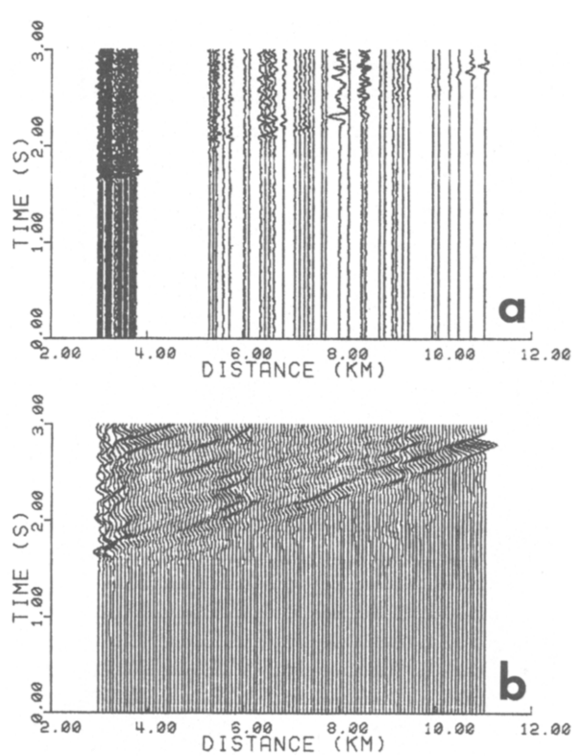


FIG. 8. Data from event 3. (a) Raw data. (b) True amplitude wave field after filtering and interpolation.

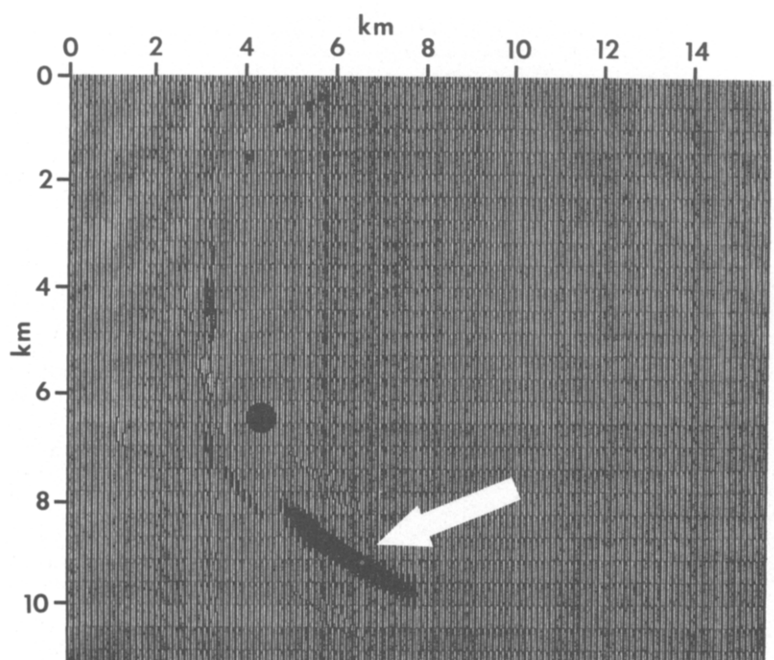


FIG. 9. The focused image from event 3. This corresponds to 600 time steps. The round black dot is the preliminary hypocenter determined from the regional network travel times. The white arrow points to the best-focused image position. Amplitudes are cubed before plotting to enhance the image.

A source image that is produced by two-dimensional extrapolation can be thought of as a planar (not necessarily vertical) slice through the focal sphere. With this in mind, we can make a direct comparison with focal parameters determined by standard methods. In Figure 10, the dotted lines are a composite of double-couple solutions for Long Valley events computed by Archuleta *et al.* (1982) and R. S. Cockerham (personal communication, 1984), and the solid lines are the compensated linear vector dipole solution computed by Julian (1983). We assume that these earlier solutions are representative of our data. The dashed line in Figure 10 corresponds to the vertical plane on which events 1 and 2 are imaged. These three solutions intersect almost at one point, which means that the imaged data do not add independent information as to whether the double-couple or compensated linear vector dipole is the more appropriate model. The plane in which the data of event 3 is extrapolated has the same strike as the dashed line in Figure 10, but dips steeply (~57.3°) to the northwest. The dip of this plane is sufficiently steep that

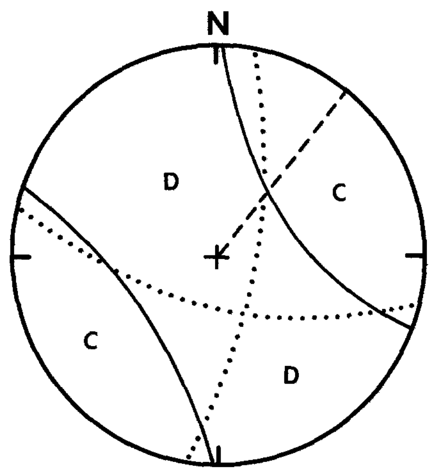


FIG. 10. Double-couple (dotted lines) and compensated linear vector dipole (solid lines) solutions for Mammoth Lakes events. Events 1 and 2 correspond to observations on a vertical slice indicated by the dashed line.

the data for this event fail to be diagnostic of the source mechanism. Nevertheless, the data show polarity reversals in the first arrivals (events 2 and 3) and nodal planes (events 1, 2, and 3). These are consistent with both the double-couple and compensated linear vector dipole solutions. All dips observed in two-dimensional images are apparent; the true dips are greater than or equal to these apparent dips.

If other considerations are equal, the relative size of the images should indicate the relative size of the events. Thus, we would say that event 3 is the largest, with an image dimension of ~3 km, followed by event 1 at ~2.5 km and event 2 at ~2 km. The corresponding body wave magnitudes are 1.45, 1.42, and 0.85, so this order is, at least quantitatively, consistent. The qualitative nature of this observation must be emphasized; by extrapolating the results of Archuleta *et al.* (1982) from larger events, the actual source dimensions are probably of the order of 100 m. If the events can be considered point sources, the relative amplitude should be used as the measure of source size.

An image may be poorly focused because of the presence of wave equation artifacts such as those due to data truncation or amplitude anomalies in the data wave field, to selection of an incorrect image time, to use of an inappropriate velocity distribution, or to an insufficiently wide aperture of observation; all of these will tend to increase the size of the image. Scattered artifacts appear in each of the source image planes, but these are typically smaller and less coherent than the source image. Energy that is not associated with the correct image tends to travel in random directions during extrapolation and so is either absorbed at the edge of the finite difference grid or has become so reduced in amplitude by spreading that the optimal image is fairly clear and unambiguous at the image time. The defocusing effects cited above tend to increase the size of the image in the direction perpendicular to propagation. A similar effect associated with aperture orientation is illustrated by Miller *et al.* (1984). The minimum size of the image in the direction of propagation is one wavelength of the dominant frequency produced by the source. Another factor that potentially contributes to artifacts in an acoustic solution is the presence of shear waves; if horizontal as well as vertical recordings were made, shear and compressional waves could be simultaneously extrapolated with an elastic solution.

## SUMMARY

The object of this paper was to demonstrate that imaging of real earthquake sources is feasible and that the resulting images are interpretable. Although this has been accomplished, it was only possible through intensive preprocessing of the data as a means of overcoming certain data deficiencies. A key consideration for the design of future experiments is how to obtain the maximum amount of independent, but usable data. By usable, we mean that the data can be interpolated the produce an unaliased wave field at the frequencies of interest. The usability criterion restricts the distance between adjacent observations. Practically, the requirement of independence translates into using as wide an aperture as possible. The aperture chosen also indirectly affects the optimal recording instrumentation. It is clearly advantageous to use identical instruments (to reduce processing requirements); thus, a wide aperture implies the desirability of a large dynamic range.

An ideal source imaging experiment would involve three-component recordings made with an areal (two-dimensional) array with extrapolation through a three-dimensional Earth model using the elastic wave equation. Such an experiment is now both conceptually and technically feasible.

## ACKNOWLEDGMENTS

G. A. M. was funded by NSF Grant EAR-8317973. The refraction data used in the determination of velocity structure were collected in projects funded by the Office of Basic Energy Science in the Department of Energy. D. P. Hill and E. Kissling offered information regarding the velocity structure of Long Valley Caldera, and D. P. Hill and P. A. Spudich provided valuable reviews. The manuscript was expertly typed by Lois Potter and Cyndi Sidles.

## REFERENCES

Alford, R. M., K. R. Kelly, and D. M. Boore (1974). Accuracy of finite-difference modeling of the acoustic wave equation, *Geophysics* **39,** 834–842.

Archuleta, R. J., E. Cranswick, C. Mueller, and P. Spudich (1982). Source parameters of the 1980 Mammoth Lakes, California, earthquake sequence, *J. Geophys. Res.* **87,** 4595–4607.

Bailey, R. A., G. B. Dalrymple, and M. A. Lanphere (1976). Volcanism, structure, and geochronology of Long Valley Caldera, Mono County, California, *J. Geophys. Res.* **81,** 725–744.

Barker, J. S. and C. A. Langston (1983). A teleseismic body-wave analysis of the May 1980 Mammoth Lakes, California, earthquakes, *Bull. Seism. Soc. Am.* **73,** 419–434.

Baumgarte, J. (1955). Konstruktive darstellung von seismischen horizonten unter berucksichtigung der strahlenbrechung im raum, *Geophys. Prosp.* **3,** 126–162.

Baysal, E., D. D. Kosloff, and J. W. C. Sherwood (1983). Reverse time migration, *Geophysics* **48,** 1514–1524.

Baysal, E., D. D. Kosloff, and J. W. C. Sherwood (1984). A two-way non-reflecting wave equation, *Geophysics* **49,** 132–141.

Claerbout, J. F. (1976). *Fundamentals of Geophysical Data Processing,* McGraw-Hill, New York.

Cramer, C. H. and T. R. Toppozada (1980). A seismological study of the May, 1980, and earlier earthquake activity near Mammoth Lakes, California, in *Mammoth Lakes, California earthquakes of May 1980,* R. W. Sherburne, Editor, *Calif. Div. Mines Geol. Spec. Rept. 150,* 91–130.

Crosson, R. S. (1976). Crustal modelling of earthquake data. 1. Simultaneous least squares estimation of hypocenters and velocity parameters, *J. Geophys. Res.* **81,** 3036–3046.

Eaton, J. P. (1966). Crustal structure in northern and central California from seismic evidence, in *Geology of Northern California,* E. H. Bailey, Editor, *Calif. Div. Mines Geol. Bull. 190,* 419–426.

Gardner, L. W. (1949). Seismograph determination of salt-dome boundary using well detector deep on dome flank, *Geophysics* **14,** 29–38.

Given, J., T. Wallace, and H. Kanamori (1982). Teleseismic analysis of the 1980 Mammoth Lakes earthquakes sequence, *Bull. Seism. Soc. Am.* **72,** 1093–1109.

Hagedoorn, J. G. (1959). The plus-minus method of interpreting seismic refraction sections, *Geophys. Prosp.* **7,** 158–182.

Hales, A. F. (1958). An accurate geophysical method for interpreting seismic refraction lines, *Geophys. Prosp.* **6,** 285–294.

Hartzell, S. (1982). Simulation of ground accelerations for the May 1980 Mammoth Lakes, California, earthquakes, *Bull. Seism. Soc. Am.* **72,** 2381–2387.

Hill, D. P. (1976). Structure of Long Valley caldera from seismic refraction experiments, *J. Geophys. Res.* **81,** 745–753.

Hill, D. P., E. Kissling, J. H. Luetgert, and U. Kradolfer (1985). Constraints on the upper crustal structure of the Long Valley-Mono Craters volcanic complex, eastern California, from seismic refraction measurements, *J. Geophys. Res.* (in press).

Johnson, L. R. (1965). Crustal structure between Lake Mead, Nevada, and Mono Lake, California, *J. Geophys. Res.* **70,** 2863–2872.

Julian, B. (1983). Mechanisms of earthquakes over Long Valley Caldera, California: evidence for dike injection, *Nature* **303,** 323–325.

Kennett, B. L. N. (1983). A new way to estimate seismic source parameters, *Nature* **302,** 659–660.

Kissling, E., W. L. Ellsworth, and R. S. Cockerham (1985). Three-dimensional structure of the Long Valley caldera, California, region by geotomography, in *Active Tectonic and Magmatic Processes Beneath Long Valley Caldera, Eastern California,* D. P. Hill, R. A. Bailey, and A. S. Ryall, Editors, *U.S. Geol. Surv., Open-File Rept. 84-939,* 188–220.

Kosloff, D. D. and E. Baysal (1983). Migration with the full acoustic wave equation, *Geophysics* **48,** 677–687.

Levin, S. (1984). Principle of reverse time migration, *Geophysics* **49,** 581–583.

Loewenthal, D. and I. R. Mufti (1983). Reversed time migration in spatial frequency domain, *Geophysics* **48,** 627–635.

Luetgert, J. H. and W. D. Mooney (1985). Crustal refraction profile of the Long Valley Caldera, California, from the January 1983 Mammoth Lakes, Earthquake swarm, *Bull. Seism. Soc. Am.* **75,** 211–221.

McMechan, G. A. (1982). Determination of source parameters by wavefield extrapolation, *Geophys. J.* **71,** 613–628.

McMechan, G. A. (1983). Migration by extrapolation of time dependent boundary values, *Geophys. Prosp.* **31,** 413–420.

Miller, D., M. Oristaglio, and G. Beylkin (1984). A new formalism and an old heuristic for seismic migration (abstract), *Expanded Abstracts with Bibliographies,* 54th Annual International SEG Meeting, Society of Exploration Geophysicists, Tulsa, Oklahoma, 704–707.

Mitchell, A. R. (1969). *Computational Methods in Partial Differential Equations,* J. Wiley and Sons, New York.

Pitt, A. M. and R. S. Cockerham (1983). Long Valley Caldera Earthquake Swarm: January 7, 1983, *Earthquake Notes* **54,** 73.

Priestley, K. F., J. N. Brune, and J. G. Anderson (1984). Surface wave excitation and source mechanism of Mammoth Lakes, California, earthquakes (abstract), *Earthquake Notes* **55,** 14.

Prodehl, C. (1979). Crustal structure of the Western United States, *U.S. Geol. Surv. Profess. Paper 1034,* 74.

Rockwell, D. W. (1967). A general wavefront method, in *Seismic Refraction Prospecting*, A. W. Musgrave, Editor, Society of Exploration Geophysicists, Tulsa, Oklahoma, 363–415.

Ryall, A. and F. Ryall (1981). Spatial-temporal variations in seismicity preceding the May 1980, Mammoth Lakes, California, earthquakes, *Bull. Seism. Soc. Am.* **71**, 747–760.

Savage, J. C., M. Lisowski, W. H. Prescott, and N. E. King (1981). Strain accumulation near the epicenters of the 1978 Bishop and 1980 Mammoth Lakes, California, earthquakes, *Bull. Seism. Soc. Am.* **71**, 465–476.

Schenck, F. L. (1967). Refraction solutions and wavefront targeting, in *Seismic Refraction Prospecting*, A. W. Musgrave, Editor, Society of Exploration Geophysicists, Tulsa, Oklahoma, 416–425.

Telford, W. M., L. P. Geldart, R. E. Sheriff, and D. A. Keys (1976). *Applied Geophysics*, Cambridge University Press, Cambridge, England.

Thornburgh, H. R. (1930). Wavefront diagrams in seismic interpretation, *Bull. Am. Assoc. Petrol. Geol.* **14**, 185–200.

Whitmore, N. D. (1983). Iterative depth migration by backward time propagation (abstract), *Expanded Abstracts with Bibliographies*, 53rd Annual International SEG Meeting, Society of Exploration Geophysicists, Tulsa, Oklahoma, 382–385.

CENTER FOR LITHOSPHERIC STUDIES
THE UNIVERSITY OF TEXAS AT DALLAS
P.O. BOX 688
RICHARDSON, TEXAS 75080 (G.A., MCM.)
CONTRIBUTION NO. 462

U.S. GEOLOGICAL SURVEY
345 MIDDLEFIELD ROAD (MS 77)
MENLO PARK, CALIFORNIA 74025 (J.H.L., W.D.M.)

Manuscript received 10 September 1984